*Journal of Modern Optics*
Vol. 53, Nos. 5–6, 20 March–15 April 2006, 739–760

Taylor & Francis
Taylor & Francis Group

# Coherent imaging with pseudo-thermal incoherent light

A. GATTI*, M. BACHE, D. MAGATTI, E. BRAMBILLA, F. FERRI and L. A. LUGIATO

INFM, Dipartimento di Fisica e Matematica, Università dell'Insubria, Via Valleggio 11, 22100 Como, Italy

(*Received 14 February 2005*)

We investigate experimentally fundamental properties of coherent ghost imaging using spatially incoherent beams generated from a pseudo-thermal source. A complementarity between the coherence of the beams and the correlation between them is demonstrated by showing a complementarity between ghost diffraction and ordinary diffraction patterns. In order for the ghost imaging scheme to work it is therefore crucial to have incoherent beams. The visibility of the information is shown for the ghost image to become better as the object size relative to the speckle size is decreased, and therefore a remarkable tradeoff between resolution and visibility exists. The experimental conclusions are backed up by both theory and numerical simulations.

## 1. Historical overview and introduction

A decade has passed since the first experimental observation of unusual interference fringes in the coincidence counts of photon pairs [1, 2]. Signal and idler photons produced by parametric down-conversion (PDC) were spatially separated and in the signal photon arm a double slit was inserted. While no first order interference pattern was visible behind the slit, an interference pattern was observed in the coincidence count by scanning the idler photon detector position. This phenomenon was given the name *ghost diffraction*. Shortly after a *ghost image* experiment was performed [3], showing a sharp image of an object placed in the signal arm by registering the coincidence counts as a function of the idler photon position.

In the interpretations of the experiments, the quantum nature of the source employed there was emphasized, although the authors of [3] suggested that "*it is possible to imagine some type of classical source that could partially emulate this behavior*". Several years passed before a systematic theory of ghost imaging (GI) started to be developed, and soon a lively debate arose discussing the role of entanglement versus classical correlation in GI schemes. In the first theoretical papers by the Boston group [4], it was claimed that entanglement was a crucial

*Corresponding author. Email: alessandra.gatti@mi.infm.it

*Journal of Modern Optics*
ISSN 0950–0340 print/ISSN 1362–3044 online © 2006 Taylor & Francis
http://www.tandf.co.uk/journals
DOI: 10.1080/09500340500147240

prerequisite for achieving GI, and in particular coherent GI: "*the distributed quantum-imaging scheme truly requires entanglement in the source and cannot be achieved using a classical source with correlations but without entanglement*." Soon after, at Rochester University a ghost image experiment was performed exploiting the classical angular correlation of narrow laser pulses [5]. This fueled the debate: which are the features of ghost imaging that truly require entanglement? The debate was continued by paper [6], where some of us showed that a classical GI scheme can indeed produce either the object image or the object diffraction pattern, but suggested that both cannot be produced without making changes to the source or the object arm setup. We argued that only entangled beams can give both results by only changing the setup in the reference arm (the one where the object is not present). While by now we know this is not true, at that time it was in partial agreement with [4] and [5]. When the Rochester group recently completed the results showing that the object diffraction pattern can be also reconstructed using classically correlated beams [7], they had indeed to change the setup (the object location, the lens setup as well as the detection protocol).

Our claim in [6] originated from the fact that only entangled beams can have simultaneously perfect spatial correlation in both the near and the far field (in both position and momentum of the photons), and no classical beams can mimic this [8]. In the same spirit, recent experimental works [7, 9, 10], brilliantly pointed out a momentum-position realization of the Einstein-Podolsky-Rosen (EPR) paradox using entangled photon pairs produced by PDC. The product of conditional variances in momentum and position was shown there to be below the EPR bound that limits the correlation of any classical (non-entangled) light beam. Based on these results, the authors of [7] proposed the same EPR bound as a limit for the product of the resolutions of the images formed in the near and in the far-field of a given classical source, and both [7, 10] argued that in ghost imaging schemes entangled photons allow a better spatial resolution to be achieved than any classically correlated beams.

This was the state of the art, when some of us had an idea leading to a ghost imaging protocol with classical thermal-like beams. Inspired by the fact that the marginal statistics of the signal or idler beam from PDC is of thermal nature, we asked ourselves what would be the result of splitting a thermal beam on a macroscopic beam splitter and using the two outgoing beams for ghost imaging. Honestly speaking, we expected at that time that this would lead to the identification of relevant differences with quantum entangled beams, where the correlation is of microscopic origin. The picture that came out was however rather different. The two output beams of the beam splitter are obviously each a true copy (on a classical level) of the input beam: if there is a speckle at some position in the input beam, then each output beam has also a speckle at the same position. Hence the beam splitter has created beams with a strong spatial correlation between them, while each beam on its own is spatially incoherent. In theoretical works [11] we showed that this correlation is preserved upon propagation (so it is present both in the near and the far-field planes), and that the beams could therefore be used to perform GI exactly in the same way as the entangled beams from PDC. Actually a very close formal analogy was demonstrated between GI with thermal and PDC beams, which implied that

classically correlated beams were able to emulate *all* the relevant features of quantum GI, with the only exception of the visibility [11].

Thus, we actually had to conclude that what we had written in [6] was not wrong but not correct either. What we failed to recognize there is that ghost imaging protocols do not need a perfect correlation at all: with the imperfect (shot-noise limited) spatial correlation of thermal beams both the object image and the object diffraction pattern can be reproduced without making any changes to the source and only changing the reference arm. Moreover, the formal analogy between thermal and PDC beams suggested that identical performances with respect to spatial resolution should be achieved by the quantum and classical protocols, provided that the spatial coherence properties of the two sources were similar. This was obviously a controversial result compared with what was published until that time [4–6] and in order to be accepted it needed an experimental confirmation. We recently provided this [12], showing high-resolution ghost image and ghost diffraction experiments performed by using a single source of pseudo-thermal speckle light divided by a beam splitter. As predicted, it was possible to pass from the image to the diffraction pattern by only changing the optical setup in the reference arm, while leaving the object arm untouched. Moreover, the product of spatial resolutions of the ghost image and ghost diffraction experiments was shown there to overcome the EPR bound which was claimed to be achievable only with entangled photons by the former literature [7, 10]. The origin of the apparent contradiction with the former literature was identified there, by recognizing that the spatial resolution of GI protocols do not coincide in general with the conditional variance, so that the product of the near and far-field resolution is free from any EPR separability bound.

The idea of using pseudo-thermal light for GI had some enthusiastic followers [13, 14] with proposals for X-ray diffraction [15], some partially converted fans, with experiments characterizing a pseudo-thermal source of photon pairs [16] and using them for realizing a ghost image [17], and some sceptics [18]. The use of pseudo-thermal light in GI schemes inspired also a topic which became of some interest, known as "quantum lithography with classical beams", or "sub-wavelength interference with classical beams". The quantum version of this started with the famous paper by Boto *et al*. [19] claiming that $N$-photon entangled states could be used for improving the resolution of lithography by a factor of $N$. A proof-of-principle experiment using $N = 2$ in the PDC case was provided by [20] where a halving of the period of the interference fringes was observed in a "ghost diffraction" pattern. In [6] some of us observed that the same effect may be observed when thermal-like beams are used, and that in both the entangled and thermal case the sub-wavelength interference relies on a simple geometrical artifact. We therefore questioned whether the Shih experiment really proved Boto's entangled protocol. Sub-wavelength interference using thermal beams was then theoretically discussed in [21], and experimentally demonstrated [22].

In this paper we continue the experimental investigations started in [12]. The main result established there was that high resolution ghost image and ghost diffraction could be achieved with the same classical source, with the product of resolutions well behind the EPR bound proposed by [7]. Here, we shall investigate

first of all a fundamental complementarity between coherence and correlation which exists for ghost imaging schemes. Only when the beams are spatially incoherent can the correlation functions allow the retrieval of information about the object (ghost image or ghost diffraction), while the information dissapears as the spatial coherence of the beams increases. This is just the opposite of what happens for direct detection of the light behind the object, where fully coherent information can be obtained only for spatially coherent beams. Thus, the spatial incoherence plays an essential role for realizing ghost imaging, while the Hanbury-Brown–Twiss interferometer [23] for determining the stellar diameter relies on coherence gained by propagation. Secondly, we will investigate visibility and signal-to-noise ratio in ghost imaging with thermal light, and highlight a tradeoff between visibility and resolution when reconstructing the information.

The paper is organized as follows: In section 2 the experiment is described, while section 3 introduces the formalism and review the formal analogy between classical and quantum ghost imaging. In addition, the relation between visibility and signal-to-noise ratio is discussed. In section 4 the spatial coherence properties of the beams are investigated and experimentally characterized. Section 5 focusses on the ghost diffraction setup and shows the complementarity between coherence and correlation. Section 6 focusses on the ghost image, and discusses visibility. In section 7 numerical results are presented which provide a more detailed insight into the results of the experiment. Finally, the conclusions are drawn in section 8.

## 2. Description of the experiment

The experimental setup is similar to that of reference [12] and is sketched in figure 1. The source of pseudo-thermal light is provided by a scattering medium illuminated by a laser beam. The medium is a slowly rotating ground glass placed in front of a scattering cell containing a turbid solution of 3 μm latex spheres. When this is illuminated with a large collimated Nd-Yag laser beam ($\lambda = 0.532\,\mu m$, diameter $D_0 \approx 10\,mm$), the stochastic interference of the waves emerging from the source

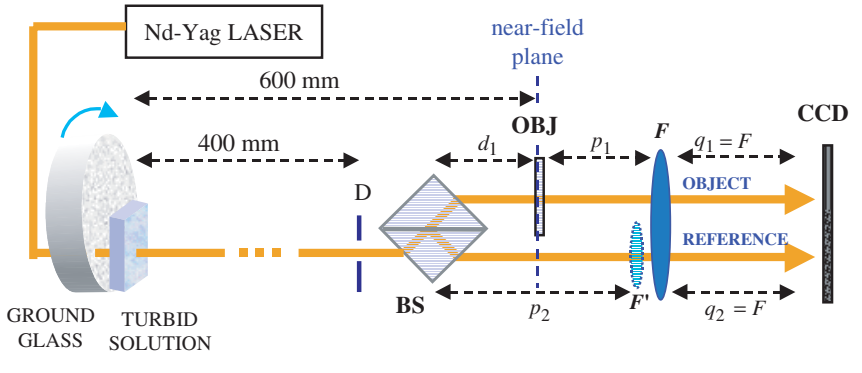


Figure 1. Scheme of the setup of the experiment (see text for details). (The colour version of this figure is included in the online version of the journal.)

produces at large distance ($z \approx 600$ mm) a time-dependent speckle pattern, characterized by chaotic statistics and by a correlation time $\tau_{coh}$ on the order of 100 ms (for an introduction to laser speckle statistics see e.g. [24]). Notice that the ground glass can be used alone to produce chaotic speckles, whose correlation time depends on the speed of rotation of the ground-glass disk and on the laser diameter, as in classical experiments with pseudo-thermal light [25, 26]. Indeed, in some part of the experiments described in the following it will be used alone. This however presents the problem that the generated speckle patterns reproduce themselves after a whole tour of the disk, which can be partially avoided by shifting laterally the disk at each tour. The turbid solution provides an easy way for generating a truly random statistics of light, because of the random motion of particles in the solution, allowing a huge number of independent patterns to be generated and used for statistics. Notice that the turbid medium cannot be used alone, because a portion of the laser light would not be scattered, thus leaving a residual coherent contribution.

At a distance $z_0 = 400$ mm from the thermal source, a diaphragm of diameter $D = 3$ mm selects an angular portion of the speckle pattern, allowing the formation of an almost collimated speckle beam characterized by a huge number (on the order of $10^4$) of speckles of size $\Delta x \approx \lambda z_0 / D_0 \approx 21$ μm [24]. The speckle beam is separated by the beam splitter (BS) into two "twin" speckle beams, that exhibit a high (although classical) level of spatial correlation [11]. The two beams emerging from the BS have slightly non-collinear propagation directions, and illuminate two different non-overlapping portions of the charged-coupled-device (CCD) camera. The data are acquired with an exposure time (1–3 ms) much shorter than $\tau_{coh}$, allowing the recording of high contrast speckle patterns. The frames are taken at a rate of 1–10 Hz, so that each data acquisition corresponds to uncorrelated speckle patterns.

In one of the two arms (the object arm 1) an object about which we need to extract information is placed. The object plane, located at a distance 200 mm from the diaphragm, will be taken as the reference plane, and referred to as the *near-field* plane (this is not to be confused with the source near-field, as the object plane is in the far zone with respect to the source). The optical setup of the object arm is kept fixed, and consists of a single lens of focal length $F = 80$ mm, placed at a distance $p_1$ after the object and $q_1 = F$ from the CCD. In this way the CCD images the far-field plane with respect to the object.

We shall consider two different setups for the reference arm 2. In the *ghost-diffraction* setup, the reference beam passes through the same lens $F$ as the object beam, located at a distance $q_2 = F$ from the CCD. In reference [12], the spatial cross-correlation function of the reference and object arm intensity distributions was calculated, and showed a sharp reproduction of the diffraction pattern of the object, comparable with the diffraction pattern obtained by illuminating the object with the laser light (see section 5).

In the *ghost-image* setup, without changing anything in the object arm, an additional lens of focal length $F'$ is inserted in the reference arm immediately before $F$. The total focal length $F_2$ of the two-lens system is smaller than its distance from the CCD, being $(1/F_2) \approx (1/F) + (1/F')$. It was thus possible to locate the position of the plane conjugate to the detection plane, by temporarily inserting the

object in the reference arm and determining the position that produced a well focussed image on the CCD with laser illumination. The object was then translated in the object arm. The distances in the reference arm obey approximately a thin lens equation of the form $1/(p_2 - d_1) + 1/q_2 \approx 1/F_2$†, providing a magnification factor $m = 1.2$. In reference [12] the intensity distribution of the reference arm was correlated with the total photon counts of the object arm showing in this case a well-resolved reproduction of the image of the object (see also section 6). Thus, the setups allows a high-resolution reconstruction of both the image and the diffraction pattern of the object by using a single source of classical light. The passage from the diffraction pattern to the image is performed by operating only on the optical setup of the reference arm, which gives evidence for the the distributed character of the correlated imaging with thermal light.

## 3. Formal equivalence of ghost imaging with thermal beams and the two-photon entangled source

The basic theory behind the setup shown in figure 1 has been explained in detail in reference [11]. The input-output relations of the beam splitter form the starting point

$$b_1(\vec{x}) = ta(\vec{x}) + rv(\vec{x}), \quad b_2(\vec{x}) = ra(\vec{x}) + tv(\vec{x}), \tag{1}$$

where $b_1$ and $b_2$ are the object and reference beams emerging from the BS, $t$ and $r$ are the transmission and reflection coefficients of the BS, $a$ is the boson operator of the speckle field and $v$ is a vacuum field uncorrelated from $a$. The state of $a$ is a thermal mixture, characterized by Gaussian field statistics, in which any correlation function of arbitrary order is expressed via the second order correlation function

$$\Gamma(\vec{x}', \vec{x}') = \langle a^{\dagger}(\vec{x}) a(\vec{x}') \rangle. \tag{2}$$

Since the collection time of our measuring apparatus is much smaller than the time $\tau_{\mathrm{coh}}$ over which the speckle fluctuates, all the beam operators are taken at equal times, and the time argument is omitted in the treatment. Notice that we are dealing with classical fields, so that the field operator $a$ could be replaced by a stochastic $c$-number field, and the quantum averages by statistical averages over independent data acquisitions. However, we prefer to keep a quantum formalism in order to outline the parallelism with the quantum entangled beams from PDC.

The fields at the detection planes are given by $c_i(\vec{x}_i) = \int \mathrm{d}\vec{x}' h_i(\vec{x}_i, \vec{x}') b_i(\vec{x}') + L_i(\vec{x}_i)$, where $L_i$ accounts for possible losses in the imaging systems, and $h_1$, $h_2$ are the impulse response functions describing the optical setups in the two arms. The object information is extracted by measuring the spatial correlation function of the intensities $\langle I_1(\vec{x}_1) I_2(\vec{x}_2) \rangle$, where $I_i(\vec{x}_i)$ are operators associated with the number of photo-counts over the CCD pixel located at $\vec{x}_i$ in the $i$th beam. All the information

†This is only approximately true because the two-lens system is equivalent to a thick lens rather than a thin lens.

about the object is contained in the correlation function of intensity fluctuations, which is calculated by subtracting the *background* term $\langle I_1(\vec{x}_1)\rangle\langle I_2(\vec{x}_2)\rangle$:

$$G(\vec{x}_1,\vec{x}_2)=\big\langle I_1(\vec{x}_1)I_2(\vec{x}_2)\big\rangle-\big\langle I_1(\vec{x}_1)\big\rangle\big\langle I_2(\vec{x}_2)\big\rangle. \tag{3}$$

The main result obtained in [11] was

$$G(\vec{x}_1,\vec{x}_2)=|tr|^2\left|\int \mathrm{d}\vec{x}_1'\int \mathrm{d}\vec{x}_2' h_1^*(\vec{x}_1,\vec{x}_1')h_2(\vec{x}_2,\vec{x}_2')\Gamma(\vec{x},\vec{x}')\right|^2, \tag{4}$$

Equation (4) has to be compared with the analogous result obtained for PDC beams [6]:

$$G_{\mathrm{pdc}}(\vec{x}_1,\vec{x}_2)=\left|\int \mathrm{d}\vec{x}_1'\int \mathrm{d}\vec{x}_2' h_1(\vec{x}_1,\vec{x}_1')h_2(\vec{x}_2,\vec{x}_2')\Gamma_{\mathrm{pdc}}(\vec{x}_1',\vec{x}_2')\right|^2, \tag{5}$$

where 1 and 2 label the signal and idler down-converted fields $a_1$, $a_2$, and

$$\Gamma_{\mathrm{pdc}}(\vec{x}_1',\vec{x}_2')=\big\langle a_1(\vec{x}_1')a_2(\vec{x}_2')\big\rangle, \tag{6}$$

is the second order field correlation between the signal and idler (also called biphoton amplitude). As already outlined in [11], ghost imaging with correlated thermal beams, described by equation (4) presents a deep analogy (rather than a duality) with ghost imaging with entangled beams, described by equation (5): (a) both are *coherent imaging systems*, which is crucial for observing interference from an object, and in particular interference from a phase object; (b) both perform similarly if the beams have similar spatial coherence properties, that is if $\Gamma$ and $\Gamma_{\mathrm{pdc}}$ have similar properties. They differ in (a) the presence of $h_1^*$ at the place of $h_1$, which implies some non fundamental geometrical differences in the setups to be used and (b) the visibility, which can be close to unity only in the coincidence count regime of PDC. We define the visibility of the information as

$$\mathcal{V}=\frac{G_{\max}}{\langle I_1I_2\rangle_{\max}}=\frac{G_{\max}}{[\langle I_1\rangle\langle I_2\rangle+G]_{\max}}. \tag{7}$$

In the thermal case $G(\vec{x}_1,\vec{x}_2)\le\langle I_1(\vec{x}_1)\rangle\langle I_2(\vec{x}_2)\rangle$ so that the visibility is never above $\frac{1}{2}$. Conversely, in the PDC case it is not difficult to verify that the ratio $G_{\mathrm{pdc}}/\langle I_1\rangle\langle I_2\rangle$ scales as $1+(1/\langle n\rangle)$, where $\langle n\rangle$ is the mean photon number per mode (see e.g. reference [11b]). Only in the coincidence-count regime, where $\langle n\rangle\ll 1$, the visibility can be close to unity, while bright entangled beams with $\langle n\rangle\gg 1$ show a similar visibility as the classical beams. However, despite never being above $\frac{1}{2}$ in the classical case, we have shown [11, 12] that the visibility is sufficient to efficiently retrieve information.

The visibility is an important parameter in determining the signal-to-noise ratio (SNR) associated with a ghost imaging scheme (see also [27]). Intuitively, one expects that the noise associated with a measurement of $I_1I_2$ is proportional to $\langle I_1I_2\rangle$, being the statistics of thermal nature. This noise also affects the retrieval of the ghost image or of the ghost diffraction in a single measurement, because this is obtained from $I_1I_2$ by subtracting the background term. Hence $\mathrm{SNR}\propto G/\langle I_1I_2\rangle$, and the visibility defined by equation (7) gives an estimate of the signal-to-noise ratio of a ghost

imaging scheme. This picture is confirmed by a more quantitative calculation, not reported here, performed by using the standard properties of Gaussian statistics. By defining $\Delta G = \sqrt{\langle O^2\rangle - \langle O\rangle^2}$, with $O = I_1 I_2 - \langle I_1\rangle\langle I_2\rangle$, where $G := G(\vec{x}_1, \vec{x}_2)$, $I_i := I_i(\vec{x}_i)$, we obtained $\Delta G \approx \sqrt{3\langle I_1 I_2\rangle^2 + 8G\langle I_1\rangle\langle I_2\rangle}$, where quantum corrections have been neglected. If the visibility is small, as it is often the case, this reduces to $\Delta G \approx \sqrt{3}\langle I_1 I_2\rangle$, and SNR $\approx (G/(\sqrt{3}\langle I_1 I_2\rangle))$.

Of course, after averaging over $N$ independent measurements $\mathrm{SNR}(N) = \sqrt{N}\mathrm{SNR}$, and if collecting a large amount of samples does not represent the problem, any ghost image/diffraction can be retrieved after a sufficient number of data collections. Hence, if the goal is retrieving information about a macroscopic stable object, the thermal source represents by far a much better deal than the entangled two-photon source. Needless to say, if the goal is performing a high sensitivity measurement, or using the ghost imaging scheme as a cryptographic scheme where information needs to be hidden to a third party, then the issue of SNR becomes crucial, and the two-photon entangled source may turn out to be the only proper choice.

## 4. Spatial coherence properties of the speckle beams

Relevant to the ghost image and the ghost diffraction schemes are the spatial coherence properties of the speckle beams in the object near-field plane, and in the far-field plane with respect to the object. These can be investigated by measuring the autocorrelation function of the intensities. In any plane it holds a Siegert-like factorization formula for thermal statistics [28, 39]:

$$\langle : I(\vec{x})I(\vec{x}') : \rangle = \big\langle I(\vec{x})\big\rangle\big\langle I(\vec{x}')\big\rangle + \frac{1}{M}\left|\Gamma(\vec{x},\vec{x}')\right|^2, \tag{8}$$

where $M$ is the degeneracy factor accounting for the number of temporal and spatial modes detected. Hence, the properties of the field correlation function $\Gamma$ can be inferred from the measurement of the intensity correlation. In particular, we will be interested in the field correlation function at the object near-field plane $\Gamma_{\mathrm{n}}(\vec{x},\vec{x}')$, and in the same function at the far-field plane $\Gamma_{\mathrm{f}}(\vec{x},\vec{x}')$.

We notice the following equalities, which are a trivial consequence of the BS input-output relations (1)

$$\langle : I_1(\vec{x})I_1(\vec{x}') : \rangle = |t|^4\langle : I(\vec{x})I(\vec{x}') : \rangle = \frac{|t|^2}{|r|^2}\langle I_1(\vec{x})I_2(\vec{x}')\rangle, \tag{9}$$

$$\langle : I_2(\vec{x})I_2(\vec{x}') : \rangle = |r|^4\langle : I(\vec{x})I(\vec{x}') : \rangle = \frac{|r|^2}{|t|^2}\langle I_1(\vec{x})I_2(\vec{x}')\rangle, \tag{10}$$

where : indicates normal ordering and $I(\vec{x})$ is the intensity distribution of the speckle beam in the absence of the BS. Apart from numerical factors, and from the shot noise contribution at $\vec{x} = \vec{x}'$, in a given plane the auto-correlation function of each of the two beams coincides with the intensity cross correlation of the two beams.

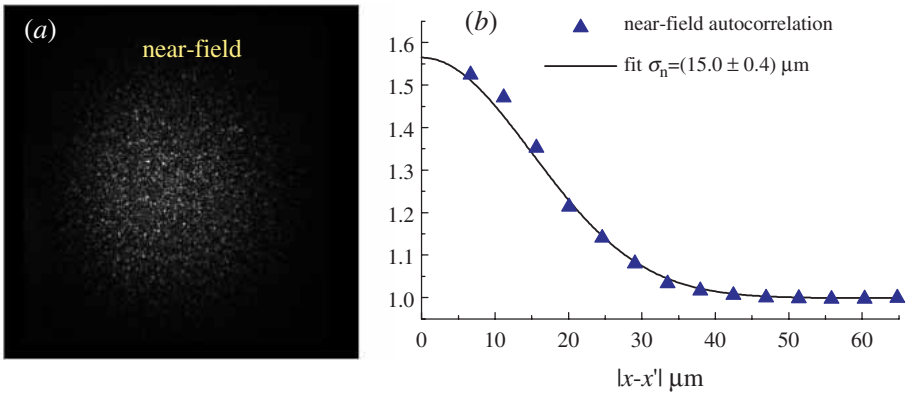


Figure 2. (*a*) Instantaneous intensity distribution $I_2$ of the speckle beam in the near-field plane; (*b*) Auto-correlation function of the intensity in (*a*). The full line is a Gaussian fit of the correlation peak, and the data have been normalized to the baseline values. (The colour version of this figure is included in the online version of the journal.)

Figure 2(*a*) shows the instantaneous intensity distribution of the reference beam in the setup of figure 1 with the lens F' inserted, so that the data recorded on the CCD are the (demagnified) image of the intensity distribution in the near-field plane. A large number of speckles are visible with a high contrast, due to the short measurement time. According to Van-Cittert Zernike theorem the size of the speckle here is determined by the inverse of the source size (the laser diameter $D_0$) and by the distance $z$ from the source [24], $\Delta x_n \propto \lambda z/D_0 = 32\,\mu m$. Frame (*b*) in this figure is the radial autocorrelation function (10), calculated as a function of the distance $|\vec{x} - \vec{x}'|$, normalized to the product of the mean intensities. The baseline corresponds to the product of the mean intensities while the narrow peak located around $|\vec{x} - \vec{x}'| = 0$ is proportional to $|\Gamma_n(\vec{x}, \vec{x}')|^2$, where $\Gamma_n$ is the second order *field* correlation function at the near-field plane. This peak reflects the spatial coherence properties of the beams at the object plane. Its width is the *near-field coherence length* $\Delta x_n$ and gives an estimate of the speckle size in this plane $\Delta x_n \approx 2m\sigma = 36\,\mu m$. Notice that the peak value is slightly smaller than twice the baseline value, giving a degeneracy factor $M = 1.7$.

Figure 3 shows the instantaneous intensity distribution (*a*) and the intensity auto-correlation function (*b*) in the far-field plane, measured in the focal plane of the lens F. The narrow peak in (*b*) located around $|\vec{x} - \vec{x}'| = 0$ is now proportional to $|\Gamma_f(\vec{x}, \vec{x}')|^2$, and its width (the *far-field coherence length*) gives an estimate of the speckle size in this plane. High-contrast speckles are visible also in the far-field plane. The Van-Cittert Zernike theorem can be again invoked to estimate their expected size, being now the source size represented by the diaphragm diameter $D$, $\Delta x_f \propto \lambda F/D \approx 14\,\mu m$ [24]. This is in good agreement with the estimation from the the correlation function, that gives $\Delta x_f = 2\sigma_f = 14.2\,\mu m$. In this case the peak value of the correlation function in frame (*b*) gives a degeneracy factor $M = 2.2$. This is slightly higher than in the near field because $\Delta x_f$ (the size of the spatial mode) is smaller and comparable with the pixel side (6.7 μm).

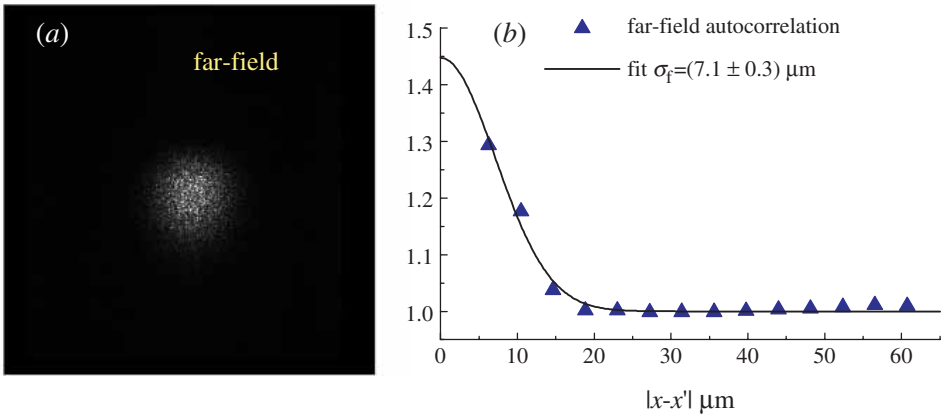


Figure 3. (*a*) Instantaneous intensity distribution of the speckles $I_1$ in the far-field plane (*b*) Auto-correlation function of the intensity in (*a*). The full line is a Gaussian fit of the correlation peak, and the data have been normalized to the baseline values. (The colour version of this figure is included in the online version of the journal.)

Because of the identities in equations (9), (10), the cross-correlation $\langle I_1 I_2 \rangle$ in the near and in the far-field coincides with the auto-correlation plotted in figure 2(*b*) and in figure 3(*b*), respectively. Hence a high degree of mutual spatial correlation is present in both planes, as a consequence of the spatial incoherence of the light produced by our source. The more incoherent is the light (the smaller the speckles with respect to the beam size), the more localized is the spatial mutual correlation function. The more coherent is the source (the larger the speckles with respect to the beam size), the flatter is the spatial mutual correlation function. As it will become clear in the next two sections, for highly spatially incoherent light, both the ghost diffraction and the ghost image can be retrieved with high resolution. Conversely, in the limit of spatially coherent light no spatial information about the object can be extracted in a ghost imaging scheme, that is from the intensity cross-correlation of the two beams as a function of the pixel position in the reference beam.

Summarizing, two aspects of our experiment are crucial (i) the spatial incoherence of light, and (ii) a measurement time $\ll \tau_{coh}$. Notice that the presence in the near-field of a large number of small speckles inside a broad beam, implies that the light is incoherent also in the far field, because $\Delta x_f \propto 1/D$, while the far-field diameter of the beam $\propto 1/\Delta x_n$.

## 5. The ghost diffraction experiment: complementarity between coherence and correlation

In this section we focus on the ghost diffraction setup (figure 1 without the lens $F'$). The object is a double slit, consisting of a thin needle of 160 μm diameter inside a rectangular aperture 690 μm wide.

In a first set of measurements the source size is $D_0 = 10$ mm, and the object is illuminated by a large number of speckles whose size $\Delta x_n = 36$ μm is much smaller

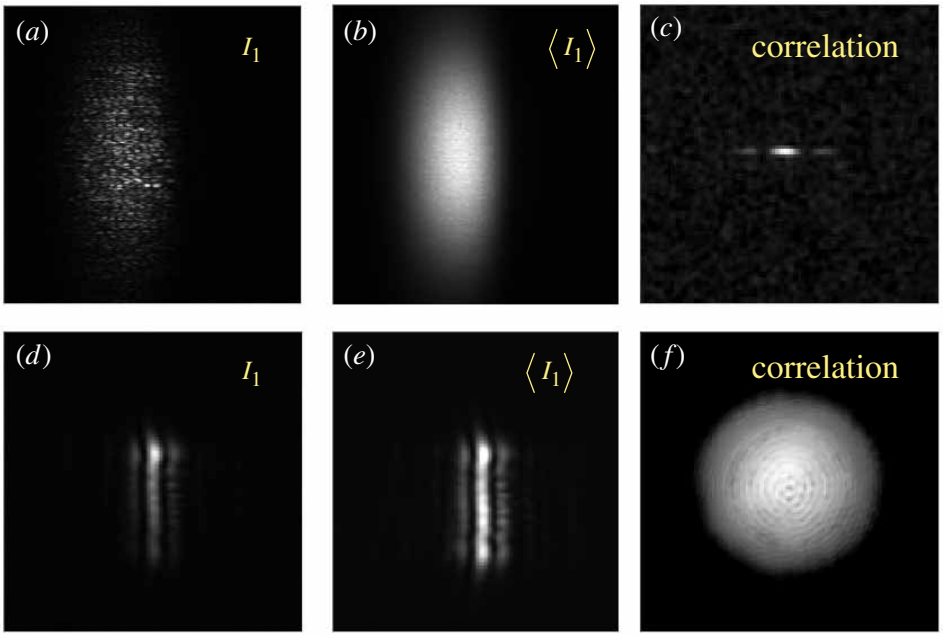


Figure 4. Ghost diffraction setup: transition from incoherent light to partially coherent light. In the three upper frames (*a–c*) the source size is $D_0 = 10\,\text{mm}$, with near-field speckles $\Delta x_n = 36\,\mu\text{m}$. In the three lower frames (*d–f*) the source size is $D_0 = 0.1\,\text{mm}$, with $\Delta x_n = 3.2\,\text{mm}$. (*a*) and (*d*): Instantaneous intensity distribution $I_1$ of the object beam. (*b*) and (*e*): Intensity distribution $\langle I_1 \rangle$, averaged over 350 shots (*c*) and (*f*): Correlation $G(\vec{x}_1, \vec{x}_2)$ as a function of $\vec{x}_2$, for a fixed $\vec{x}_1$, averaged over 20 000 shots.

than the slit separation. The light is *spatially incoherent* as described in the previous section. The results are shown in the first row of figure 4. Frame (*a*) is the instantaneous intensity distribution of the object beam, showing a speckled pattern, with no interference fringes from the double slit, as expected for incoherent illumination [28]. At a closer inspection, the shape of the speckles resembles the interference pattern of the double slit, but since these speckles move randomly in the transverse plane from shot to shot, an average over several shots displays a homogeneous broad spot (figure 4(*b*)). Frame (*c*) is a plot of $G(\vec{x}_1, \vec{x}_2)$ as a function of the reference pixel position $\vec{x}_2$, and shows the result of correlating the intensity distribution in the reference arm with the intensity collected from a single fixed pixel in the object arm. Notice that at difference to what was done in [12], no spatial average [30] is employed here: this makes the convergence rate slower but the scheme is closer to the spirit of ghost diffraction in which the information is retrieved by only scanning the reference pixel position. The *ghost diffraction* pattern emerges after a few thousands of averages, and is well visible after 20 000 averages. This is confirmed by the data of figure 5(*a*) which compare the horizontal section of the diffraction pattern from a correlation measurement with that obtained with laser illumination.

In a second set of measurements the source size is reduced to $D_0 = 0.1\,\text{mm}$, by inserting a small pinhole after the ground glass. As a result, the spatial coherence of

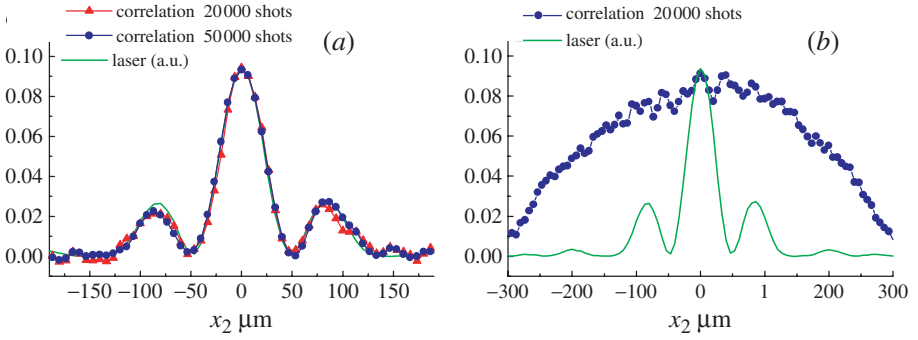


Figure 5. Horizontal sections of the correlation $G(\vec{x}_1, \vec{x}_2)$ as a function of $x_2$, for a fixed $\vec{x}_1$ (see figure 4(*c*), (*f*)). (*a*) Is the case of incoherent light, $D_0 = 10$ mm; the data are obtained with an average over 20 000 shots (triangles) and 50 000 shots (circles). (*b*) Is the case of partially coherent illumination, $D_0 = 0.1$ mm (20 000 shots). The light full line is for comparing the diffraction pattern observed with a laser. (The colour version of this figure is included in the online version of the journal.)

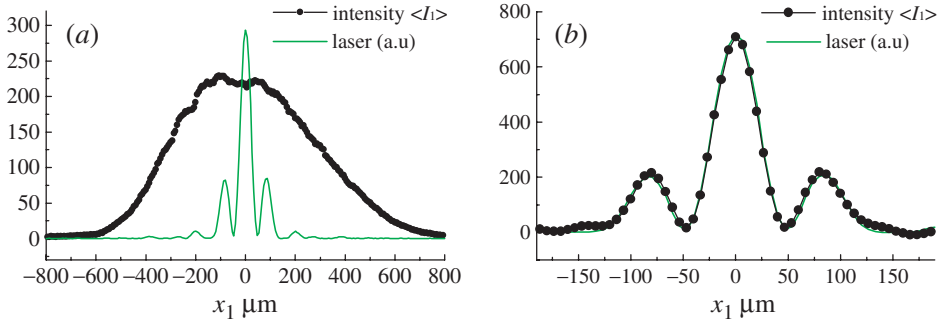


Figure 6. Horizontal sections of the average intensity distribution $\langle I_1(\vec{x}_1)\rangle$ in the object arm (see figure 4(*b*), (*e*)). (*a*) Is obtained for incoherent light, with $D_0 = 10$ mm (350 shots), while (*b*) plots the case of partially coherent illumination, with $D_0 = 0.1$ mm (500 shots). The light full line is for comparing the diffraction pattern observed with a laser. (The colour version of this figure is included in the online version of the journal.)

the light illuminating the object is increased. As the speckle size at the diaphragm $D$ is now $\approx 3$ mm , on average the object is illuminated by a single speckle of size much larger than the slit separation. The results are reported in the second row of figure 4. As expected [28] the interference fringes are now visible in the instantaneous intensity distribution of the object beam 1 [frame (*d*)], and become sharper after averaging over some hundreds of shots [frame (*e*)]. Notice that the shape of the interference pattern is now elongated in the vertical direction, because the light emerging from the small source is not collimated. Horizontal sections of $\langle I_1\rangle$, plotted in figure 6(*b*), show a very good agreement with the diffraction pattern from laser illumination. Instead, no interference fringes at all appear in the correlation function of the intensities in the two arms, when plotted as a function of $\vec{x}_2$ [frame (*f*)]. Notice that in this set of measurements the turbid medium was removed in order to increase the power. This is feasible in this case, because the very small size of the source allows

a large number of independent patterns to be generated in a single tour of the glass disk.

Figures 4, 5, and 6 evidence a remarkable complementarity between the observation of interference fringes in the correlation function (ghost diffraction), and in the intensity distribution of the object beam (ordinary diffraction). It also shows the fundamental role played by the spatial incoherence of the source in producing a ghost diffraction pattern: the more incoherent is the source, the more the two beams are spatially correlated and the more information about the object is available in the ghost diffraction pattern. The more coherent is the source, the flatter is the spatial correlation function of the two beams and the less information about the object is contained in the ghost diffraction. This is completely analogous to the complementarity between the one-photon and two-photon interference in Young's double slit experiments with photons from a PDC source [31], which was explained as a complementarity between coherence and entanglement. In our case of thermal beams, the complementarity is rather between coherence and spatial correlation, showing that also in this respect the classical spatial correlation produced by splitting thermal light plays the same role as entanglement of PDC photons.

These results can be easily understood by using the formalism developed in section 3, and in particular by inspection of equation (4) for the correlation function of the intensity fluctuations $G(\vec{x}_1, \vec{x}_2)$. In the limit of spatially coherent light the field correlation function $\Gamma_n(\vec{x}_1, \vec{x}_2)$ becomes constant in space in the region of interest, and the two integrals in equation (4) factorize into the product of two ordinary imaging schemes, showing the diffraction pattern of the object only in the object arm 1. As a result, by plotting the correlation as a function of $\vec{x}_2$, no object diffraction pattern can be observed, that is, no ghost diffraction occurs. The same observation can be made with respect to $\Gamma_{pdc}(\vec{x}_1, \vec{x}_2)$, and $G_{pdc}(\vec{x}_1, \vec{x}_2)$, explaining thus the analogy between the role of light coherence in the PDC and in the thermal case.

In general, the result of a correlation measurement is obtained by inserting into equation (4) the propagators that describe the ghost diffraction setup: $h_1(\vec{x}_1, \vec{x}_1') = (i\lambda F)^{-1} e^{-((2\pi i)/\lambda F)\vec{x}_1 \cdot \vec{x}_1'} T(\vec{x}_1')$, with $T(\vec{x})$ being the object transmission function, and $h_2(\vec{x}_2, \vec{x}_2') = (i\lambda F)^{-1} e^{-((2\pi i)/\lambda F)\vec{x}_2 \cdot \vec{x}_2'}$. We get

$$G(\vec{x}_1, \vec{x}_2) \propto \left| \int d\vec{\xi}\, \tilde{T}\left[ (\vec{x}_1 - \vec{\xi}) \frac{2\pi}{\lambda F} \right] \Gamma_f(\vec{x}_2, \vec{\xi}) \right|^2, \tag{11}$$

where $\tilde{T}(\vec{q}) = \int (d\vec{x}/2\pi) e^{-i\vec{q}\cdot\vec{x}} T(\vec{x})$ is the amplitude of the diffraction pattern from the object. The result of a correlation measurement is a convolution of the diffraction pattern amplitude with the second order correlation function in the far-field. Hence the *far-field coherence length* determines the spatial resolution in the ghost diffraction scheme: the smaller the far-field speckles, the better resolved is the pattern. In the limit of speckles much smaller than the scale of variation of the diffraction pattern

$$G(\vec{x}_1, \vec{x}_2) \to \left| \tilde{T}\left[ (\vec{x}_1 - \vec{x}_2) \frac{2\pi}{\lambda F} \right] \right|^2 \left| \int d\vec{\xi} \Gamma_f(\vec{\xi}, \vec{x}_2) \right|^2. \tag{12}$$

Since the Fourier transform of the amplitude of the object transmission function is involved in equation (11), ghost diffraction of a pure phase object can be realized

with spatially incoherent pseudo-thermal beams, a possibility which was questioned in a recent letter [18].

## 6. The ghost image: tradeoff between resolution and visibility

By simply inserting the lens $F'$ in the reference arm (see figure 1), without changing anything in the object arm, we now pass to the ghost image. As predicted in [11], and experimentally demonstrated in [12], the result of cross-correlating the intensities of the reference and object arm is now the image of the object, shown e.g. in figure 7(*a*).

Two issues are important in any imaging scheme: the spatial resolution and the signal-to-noise ratio.

As pointed out in [11, 12], the resolution capabilities of the ghost image setup are determined by the near field coherence length $\Delta x_n$ (the size of the near-field speckles). This can be easily understood by inserting the propagator $h_2(\vec{x}_2, \vec{x}'_2) = m\delta(m\vec{x}_2 + \vec{x}'_2)$, into equation (4):

$$G(\vec{x}_1, \vec{x}_2) \propto \left| \int d\vec{x}'_1 \Gamma_n(\vec{x}'_1, -m\vec{x}_2) T^*(\vec{x}'_1) e^{i(2\pi/\lambda f)\vec{x}_1 \cdot \vec{x}'_1} \right|^2, \tag{13}$$

which shows that the result of a correlation measurement in this setup is a convolution of the object transmission function with the near-field correlation function $\Gamma_n$. In the following we shall consider a *bucket* detection scheme, where the reference beam intensity $I_2$ is correlated with the total photon counts in the object arm, that is, in practice with the sum of photo counts over a proper set of pixels. This makes the imaging incoherent [30], because it amounts to measuring

$$\int d\vec{x}_1 G(\vec{x}_1, \vec{x}_2) = \int d\vec{x}'_1 \left|\Gamma_n(\vec{x}'_1, -m\vec{x}_2)\right|^2 \left|T(\vec{x}'_1)\right|^2. \tag{14}$$

If we take the limit of spatially coherent light, where $\Gamma_n(\vec{x}'_1, -m\vec{x}_2)$ can be considered as constant over the whole beam size, both equations (13) and (14) show that no information about the object image can be obtained by scanning $\vec{x}_2$. Conversely in the limit of spatially incoherent light where the speckle size is much smaller than the scale of variation of the object, $\Gamma_n(\vec{x}'_1, -m\vec{x}_2) \approx \delta(\vec{x}'_1 + m\vec{x}_2)$, and both equations (13) and (14) converge to $|T(-m\vec{x}_2)|^2 \times \text{const}$.

Concerning the signal-to-noise ratio, the discussion in section 3 pointed out that it was determined by the image visibility. We have studied the visibility of the ghost image of a double slit in a sequence of measurements where the vertical size of the apertures was progressively reduced, while leaving unchanged their horizontal size and separation. This is shown in figure 7(*a*), where all the frames display the correlation function measured in a bucket detection scheme as a function of the reference pixel position $\vec{x}_2$. Despite the fact that all the frames have been obtained with the same number of averages $N = 10\,000$, the sequence displays a remarkable enhancement of the visibility as the object area is reduced.

This enhancement is more clearly visible in the horizontal sections plotted in figure 7(*b*), where in each point the correlation function has been normalized to

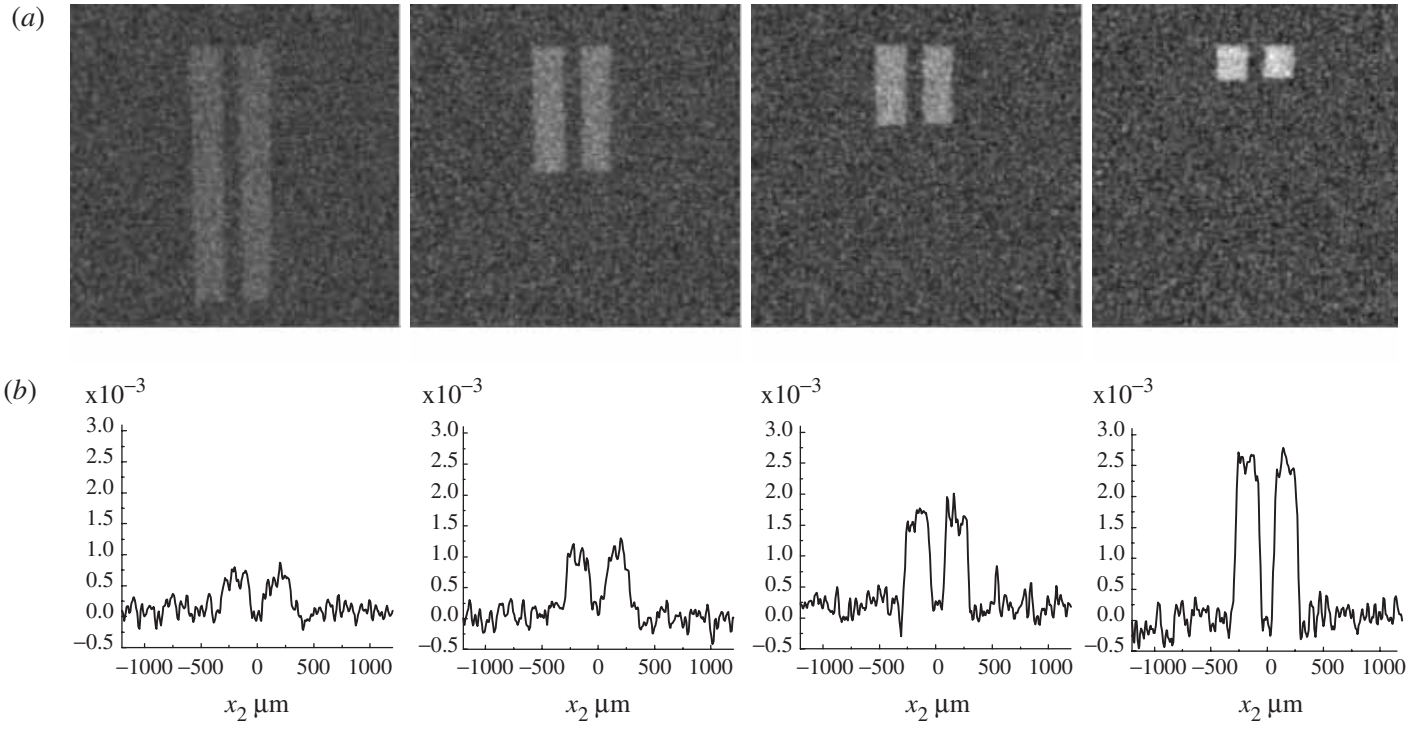


Figure 7. Reconstruction of the object image via correlation measurements (figure 1, with the lens $F'$ inserted). (*a*) Cross-correlation of the intensity distribution of the reference arm with the total photo counts in the object arm, as a function of $\vec{x}_2$ (statistics over 10 000 CCD frames). In the sequence of frames the object area is progressively reduced, and correspondingly an enhancement of the visibility can be observed. (*b*) Horizontal sections of the images in (*a*), with the correlation normalized to $\langle I_1 I_2 \rangle$, so that the vertical scales give the visibility.

$\langle I_1 I_2 \rangle$, so that the numbers on the vertical axis give directly the visibility [see equation (7)]. We notice that the visibility increases as the object area decreases, and correspondingly the signal-to-noise-ratio increases, as expected.

In order to understand the origin of the behaviour shown in figure 7, we need first to consider equation (14), that gives the correlation function in the bucket detection scheme. Let us assume that the object simply transmits the light over a region of area $S_{\mathrm{obj}}$ and stops it elsewhere. By assuming that the coherence length $\Delta x_{\mathrm{n}}$ is smaller than the object features, as it is necessary for the object to be resolved, the integrand on the r.h.s of (14) can be non-zero for $\vec{x}_1'$ in a region located around $\vec{x}_2$, of area $A_{\mathrm{coh}}$, where $A_{\mathrm{coh}}$ is the *coherence area* $\propto \Delta x_{\mathrm{n}}^2$. Thus the correlation scales as the coherence area.

$$\int \mathrm{d}\vec{x}_1 G(\vec{x}_1, \vec{x}_2) \propto A_{\mathrm{coh}}. \tag{15}$$

Conversely, it is not difficult to see that in the bucket detection scheme

$$\int \mathrm{d}\vec{x}_1 \langle I_1(\vec{x}_1) \rangle = \int \mathrm{d}\vec{x}_1' \left| T(\vec{x}_1') \right|^2 \langle I_n(\vec{x}_1') \rangle \propto A_{\mathrm{obj}}, \tag{16}$$

where $\langle I_n(\vec{x}_1') \rangle$ is the average intensity distribution of the light illuminating the object, that can be taken as roughly uniform on the object area (the speckles average to a broad uniform light spot, as shown in figure 4(*b*)). Hence the ratio of the correlation to the background scales as:

$$\frac{\int \mathrm{d}\vec{x}_1 G(\vec{x}_1, \vec{x}_2)}{\int \mathrm{d}\vec{x}_1 \langle I_1(\vec{x}_1) \rangle \langle I_2(\vec{x}_2) \rangle} \propto \frac{A_{\mathrm{coh}}}{A_{\mathrm{obj}}}. \tag{17}$$

This formula is reminiscent of the role of the mode degeneracy in equation (8), and indeed it reflects the fact that in a bucket detection scheme the number of spatial modes detected is proportional to $A_{\mathrm{obj}}/A_{\mathrm{coh}}$, which represents a degeneracy factor that reduces the visibility of the correlation with respect to the background. The ratio in equation (17) is usually small, so that the visibility of the ghost image roughly coincides with it. Thus the visibility roughly scales as the ratio of the coherence area to the object transmissive area: the larger are the object dimensions with respect to the speckles, that is, the more incoherent is the light illuminating the object, the worse is the visibility of the ghost image. This is confirmed by the plot in figure 8, showing how the visibility increases with the inverse of the object area. This rather counter-intuitive result also implies that a better resolution can be achieved only at the expenses of the visibility, since the resolution is determined by the speckle size. Hence, complex images that need small speckles to be resolved in their details have a lower signal-to-noise ratio than simple images which can be resolved with relatively large speckles (see also [17] for a similar conclusion).

This, however, does not prevent from retrieving more complex images (see e.g. figure 9), provided that a larger number of data acquisitions are performed.

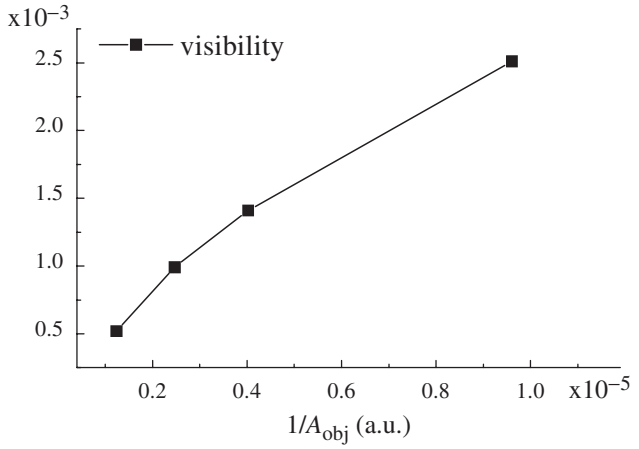


Figure 8. Visibility of the ghost image as a function of the inverse of the transmissive area of the object, showing an increase of the visibility by reducing the object area.

Figure 9. Ghost image of the number 4, retrieved from the correlation function after averaging over 30 000 shots.

## 7. Numerical results

In this section we use a numerical model for simulating the speckle pattern created by the ground glass and the turbid medium to support the results of the previous section. The thermal field is created by generating a noisy field with huge phase fluctuations. We then multiply the noisy field with a Gaussian profile and a subsequent Fourier transformation gives what corresponds to the near field; the width of the Gaussian then controls the near-field speckle size. The far-field speckle size is controlled independently as in the experiment: after generating the near field, a diaphragm of diameter $D$ is introduced, beyond which only vacuum fluctuations appear; $D$ then controls the far-field speckle size. The speckle field transmitted by the diaphragm is then impinged on a 50/50 BS, with vacuum fluctuations entering the unused port, giving the two desired correlated beams. We neglect the temporal statistics, since we assume that the short measurement time of the experiment

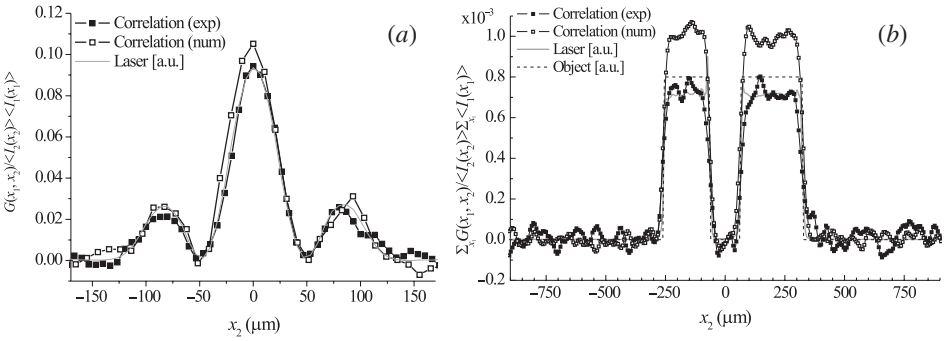


Figure 10. Comparing a two dimensional numerical simulation of the experiment, by showing the correlation of intensity fluctuations normalized to the product of the beam intensities. (*a*) The ghost diffraction case $G(\vec{x}_1,\vec{x}_2)/\langle I_1(\vec{x}_1)\rangle\langle I_2(\vec{x}_2)\rangle$. (*b*) The ghost image case $\int \mathrm{d}x_1 G(x_1,x_2)/\langle I_2(x_2)\rangle \int \mathrm{d}x_1\langle I_1(x_1)\rangle$. In both cases the numerics and experiment are real units, and are as reference compared with the data obtained by coherent laser illumination of the object. The averages are done over $2\cdot 10^4$ realizations. In the numerics $\Delta x_\mathrm{n} = 34\,\mu\mathrm{m}$ and $\Delta x_\mathrm{f} = 12\,\mu\mathrm{m}$.

provides a speckle pattern frozen in time. We should finally mention that a Wigner formalism is used to describe the quantized fields, as described in detail in [8].

Initially, let us briefly show that the numerical simulations are able to describe very precisely the experiment. In figure 10 are shown the results of two-dimensional (2D) simulations with all parameters kept as close as possible to the experiment. These include near-field and far-field speckle sizes, object and aperture sizes, as well as a number of realizations. Both the ghost diffraction pattern [figure 10(*a*)] and the ghost image (figure 10(*b*)) show a very good agreement with the experimental recorded data (using the small-speckle setup of sections 4–6). We stress that this comparison is not in arbitrary units.

In section 5 we showed experimentally the behaviour of the system when using either coherent or incoherent beams to investigate the diffraction properties of an object. In order to investigate better the actual transition from coherent to incoherent illumination of the object, we have carried out numerical simulations that are presented in figure 11. We have kept $D = 3\,\mathrm{mm}$ there and then for each simulation changed $\Delta x_\mathrm{n}$. The simulation only includes one spatial direction (1D), and therefore the coherence properties of the beam are governed by the ratio $\Delta x_\mathrm{n}/L_\mathrm{obj}$, where $L_\mathrm{obj}$ is the 1D equivalent of $A_\mathrm{obj}$. Thus, the smaller $\Delta x_\mathrm{n}/L_\mathrm{obj}$ the more incoherent is the beam impinging on the object. For small speckles ($\Delta x_\mathrm{n}/L_\mathrm{obj} \ll 1$) the beams are spatially incoherent, implying a strong spatial correlation between the beams: the ghost diffraction is observed in the correlation [figure 11(*a*)]. In contrast, no diffraction pattern can be observed directly in the object beam [figure 11(*b*)]. As $\Delta x_\mathrm{n}$ is increased by generating bigger speckles the beams become more and more spatially coherent ($\Delta x_\mathrm{n}/L_\mathrm{obj} \simeq 1$): the ghost diffraction disappears gradually (figure 11(*a*)), while the diffraction pattern starts to appear from the direct observation of the object beam (figure 11(*b*)). Figure 11(*c*) shows what happens to the ghost image during this transition: the incoherence for

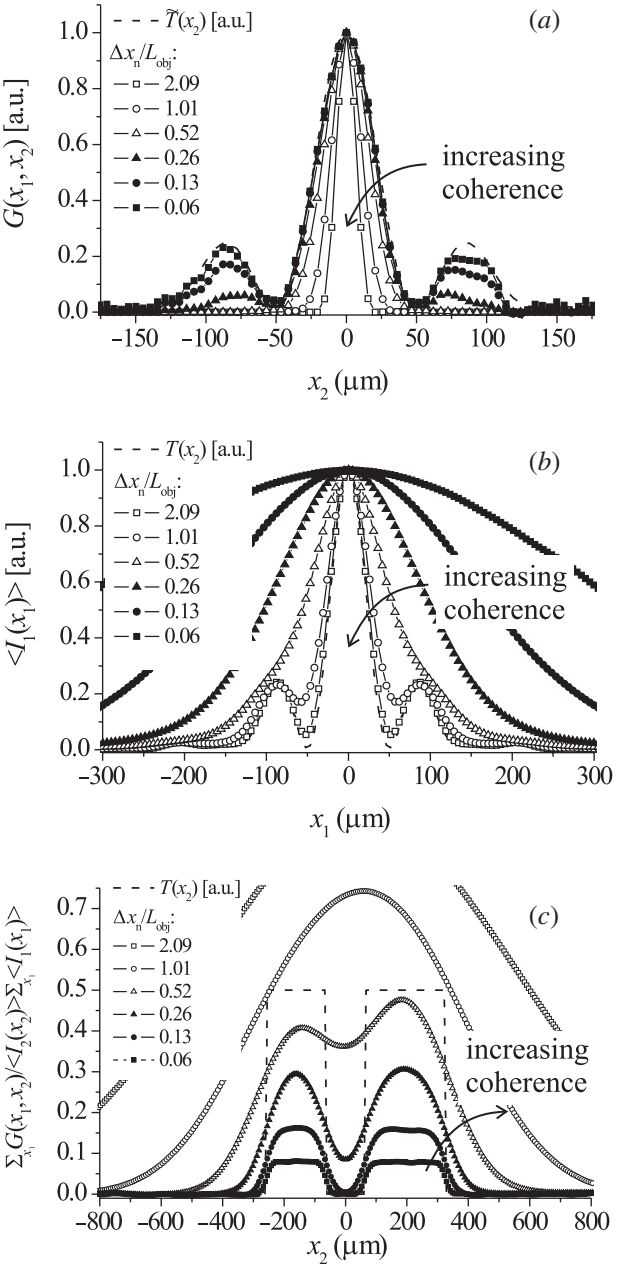


Figure 11. 1D numerical simulation of the experiment showing the transition from incoherent to coherent illumination of the object, realized by changing the near-field speckle size $\Delta x_n$. (*a*) Shows the normalized correlation of intensity fluctuations in the ghost diffraction case, while (*b*) shows the normalized $\langle I_1(x_1)\rangle$ as observed directly in the object arm. (*c*) Shows the correlation of intensity fluctuations in the ghost image case, normalized to the beam intensities $\int dx_1 G(x_1, x_2)/\langle I_2(x_2)\rangle \int dx_1 \langle I_1(x_1)\rangle$. The averages are done over $10^5$ realizations. The object mimics the experimental one, implying $L_{obj} = 530\,\mu m$. $\Delta x_f = 12\,\mu m$.

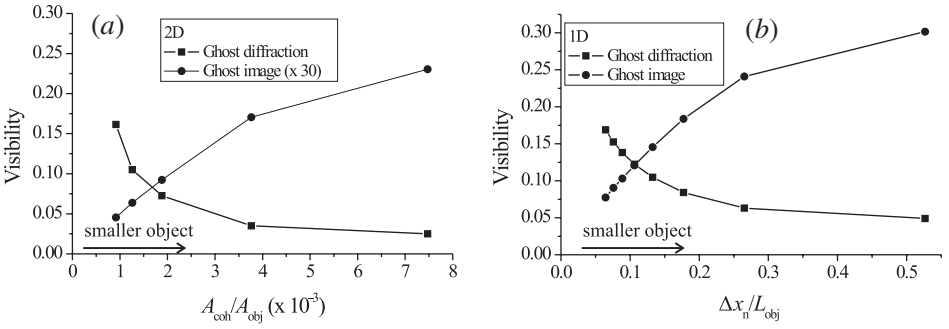


Figure 12. Numerical simulations of the experiment showing how the object size affects the visibility $V$. We kept the speckle sizes constant but varied the width of the two slits: (*a*) is the 2D case showing $V$ as function of the speckle area relative to the object area. Note that the ghost image visibility has been multiplied by a factor of 30, and that the object length perpendicular to the slits was kept constant; (*b*) is the 1D case, showing $V$ as function of the speckle size relative to the object length. $\Delta x_n = 34\,\mu m$ and $\Delta x_f = 12\,\mu m$.

small $\Delta x_n$ implies that a ghost image of the object can be observed, and this image disappears gradually while increasing the coherence.

We saw in section 6 that the visibility of the ghost image became better as the object area was reduced, cf. figure 8. To investigate this phenomenon in general we show in figure 12 how the object size† affects the visibility of the information. The trend we saw in the experiment is repeated in the numerics: in figure 12(*a*) the ghost image visibility increases as the object size decreases because fewer modes are transmitted. In figure 12(*b*) the simulation is repeated for the 1D case with a similar result. However, since in the 1D case much fewer modes are transmitted by the object the visibility is much higher. We have also in figure 12 plotted the visibility of the ghost diffraction fringes, and we observe that–in contrast to the ghost image case–the visibility decreases as the object size is decreased (a result reported also in [13]). This is is to be expected because for the diffraction pattern the modes transmitted by the object interfere coherently so $G(\vec{x}_1, \vec{x}_2) \propto A_{obj}^2$ (for the 2D case). In contrast, for the mean intensity the modes interfere incoherently so $\langle I_1(\vec{x}_1)\rangle \propto A_{obj}$. Thus $G(\vec{x}_1, \vec{x}_2)/\langle I_1(\vec{x}_1)\rangle\langle I_2(\vec{x}_2)\rangle \propto A_{obj}$: the bigger the object the better the visibility of the information. We also note that there is basically no difference between the 1D and 2D results for the ghost diffraction visibility. This is because a similar argument can be done for the 1D case showing $G(x_1, x_2)/\langle I_1(x_1)\rangle\langle I_2(x_2)\rangle \propto L_{obj}$. Finally, we have checked that if the far-field speckle size $\Delta x_f$ is varied and all other parameters are kept fixed, then the visibility of the diffraction fringes increases as $\Delta x_f$ is increased: again a tradeoff between resolution and visibility is found.

†Note that here we keep the length perpendicular to the slits constant but vary the width of the slits. Experimentally, this would correspond to maintaining the needle but changing the width of the surrounding aperture.

## 8. Conclusions

The experimental results reported in this paper confirm that correlated imaging can be performed with a classical thermal source. A remarkable complementarity between spatial coherence and correlation is predicted and confirmed by experiments and numerical simulations. By changing the coherence of the speckle field at the object plane from incoherent to coherent (measured relative to the object dimensions), the object diffraction pattern reconstructed from correlations disappears but appears in the far field intensity distribution measured in the object arm. We also discussed from a quantitative point of view the issue of the visibility of the correlated imaging scheme. We showed that the visibility of the object image was proportional to the ratio between the object area and the field coherence area at the object plane. This means that a tradeoff between resolution and visibility exists: a better visibility can be obtained only at the expense of a lower resolution and vice versa. However, the experiment clearly shows that a fairly good resolution can be achieved since the problem of low visibility can be overcomed by performing a sufficiently large number of averages.

## Acknowledgments

This work was carried out under the framework of the FET project QUANTIM of the EU, of the PRIN project of MIUR ''Theoretical study of novel devices based on quantum entanglement'', and of the INTAS project ''Non-classical light in quantum imaging and continuous variable quantum channels''. M.B. acknowledges financial support from the Carlsberg Foundation.

## References

[1] D.V. Strekalov, A.V. Sergienko, D.N. Klyshko, *et al.*, Phys. Rev. Lett. **74** 3600 (1995).
[2] P.H. Souto Ribeiro, S. Padua, J.C. Machado da Silva, *et al.*, Phys. Rev. A **49** 4176 (1994).
[3] T.B. Pittman, Y.H. Shih, D.V. Strekalov, *et al.*, Phys. Rev. A **52** R3429 (1995).
[4] A.F. Abouraddy, B.E.A. Saleh, A.V. Sergienko, *et al.*, Phys. Rev. Lett. **87** 123602 (2001); J. Opt. Soc. Am. B **19** 1174 (2002).
[5] R.S. Bennink, S.J. Bentley and R.W. Boyd, Phys. Rev. Lett. **89** 113601 (2002).
[6] A. Gatti, E. Brambilla and L.A. Lugiato, Phys. Rev. Lett. **90** 133603 (2003).
[7] R.S. Bennink, S.J. Bentley, R.W. Boyd, *et al.*, Phys. Rev. Lett. **92** 033601 (2004).
[8] E. Brambilla, A. Gatti, M. Bache, *et al.*, Phys. Rev. A **69** 023802 (2004).
[9] J.C. Howell, R.S. Bennink, S.J. Bentley, *et al.*, Phys. Rev. Lett. **92** 210403 (2004).
[10] M. D'Angelo, Y.-H. Kim, S.P. Kulik, *et al.*, Phys. Rev. Lett. **92** 233601 (2004), quant-ph/0401007.
[11] (a) A. Gatti, E. Brambilla, M. Bache, *et al.*, Phys. Rev. Lett. **93** 093602 (2004), quant-ph/0307187; (b) Phys. Rev. A **70** 013802 (2004), quant-ph/0405056.
[12] F. Ferri, D. Magatti, A. Gatti, *et al.*, Phys. Rev. Lett. **94** 183602 (2005); D. Magatti, F. Ferri, A. Gatti, *et al.*, quant-ph/0408021.
[13] Y. Cai and S.-Y. Zhu, Optics Letters **29** 2716 (2004).
[14] D.-Z. Cao, Z. Li, Y.-H. Zhai, *et al.* (2004), quant-ph/0401109.
[15] J. Cheng and S. Han, Phys. Rev. Lett. **92** 093903 (2004).

[16] G. Scarcelli, A. Valencia and Y. Shih, Phys. Rev. A **70** 051802(R) (2004), quant-ph/0409210.
[17] A. Valencia, G. Scarcelli, M. D'Angelo, *et al.* (2004), quant-ph/0408001.
[18] A.F. Abouraddy, P.R. Stone, A.V. Sergienko, *et al.*, Phys. Rev. Lett. **93** 213903 (2004).
[19] A.N. Boto, P. Kok, D.S. Abrams, *et al.*, Phys. Rev. Lett. **85** 2733 (2000).
[20] M. D'Angelo, M.V. Chekhova and Y. Shih, Phys. Rev. Lett. **87** 013602 (2001).
[21] K. Wang and D.-Z. Cao, Phys. Rev. A **70** 041801R (2004), quant-ph/0404078.
[22] G. Scarcelli, A. Valencia and Y. Shih, Europhys. Lett. **68** 618 (2004), quant-ph/0410217.
[23] R. Hanbury-Brown and R.Q. Twiss, Nature (London) **177** 27 (1956).
[24] J.W. Goodman, in *Laser speckle and related phenomena*, Vol. 9 of *Topics in Applied Physics*, edited by D. Dainty (Springer, Berlin, 1975), p. 9.
[25] W. Martienssen and E. Spiller, Am. J. Phys. **32** 919 (1964).
[26] F.T. Arecchi, Phys. Rev. Lett. **15** 912 (1965).
[27] J. Cheng and S. Han (2004), quant-ph/0408123.
[28] L. Mandel and E. Wolf, *Optical coherence and quantum optics* (Cambridge, New York, 1995).
[29] J.W. Goodman, *Statistical optics* (Wiley Classic Library, New York, 2000).
[30] M. Bache, E. Brambilla, A. Gatti, *et al.*, Opt. Express **12** 6067 (2004), quant-ph/0409215.
[31] A.F. Abouraddy, M.B. Nasr, B.A. Saleh, *et al.*, Phys. Rev. A **63** 063803 (2001).